An Automated Workflow for Reliable Focal Mechanism Determination of Low-Magnitude Earthquakes in the Southeastern Alps

Fatemeh Abdi[*1], Angela Saraò[1], Andrea Magrin[1], Monica Sugan[1], Laura Cataldi[1], Giovanni Messuti[2,3], Giuliana Rossi[1], and Matteo Picozzi[1]

Abstract

In regions dominated by low-magnitude seismicity, obtaining reliable focal mechanisms (FMs) at the catalog scale remains challenging, particularly when waveform-based inversions are limited by simplified velocity models and network geometry. Here, we present an automated workflow for polarity-based FM determination that combines deep-learning first-motion classification using the convolutional first-motion model with probabilistic inversion through SKHASH, accounting for uncertainties in source location, velocity structure, and polarity assignment. Once event locations and *P*-wave arrivals are available, the workflow requires no manual polarity review and provides quantitative quality metrics for solution robustness. The workflow is validated against a reference focal-mechanism catalog of 159 earthquakes with manually reviewed polarities, used here as a validation dataset. Automated polarity classifications agree with manual picks in 92% of cases, and 73% of the resulting FMs differ by less than 30° in Kagan angle from the reference solutions, demonstrating reliable performance for small-magnitude events. We apply the workflow to approximately 1500 earthquakes recorded in northeastern Italy between 2024 and 2025 ($1.0 \le M_d \le 4.6$), yielding 122 quality-controlled FMs, consistent with the established seismotectonic framework of the southeastern Alps, and producing the first automated FM catalog for this region. Nearly 75% of the retained solutions correspond to earthquakes with $M_d \le 2.5$, significantly densifying the available FM dataset at small magnitudes. An additional application to the 2025 Raveo earthquake sequence confirms the consistency of the automated solutions with independently derived moment tensor and manual focal mechanism results.

Cite this article as Abdi, F., A. Saraò, A. Magrin, M. Sugan, L. Cataldi, G. Messuti, G. Rossi, and M. Picozzi (2026). An Automated Workflow for Reliable Focal Mechanism Determination of Low-Magnitude Earthquakes in the Southeastern Alps, *Seismol. Res. Lett.* **XX**, 1–16, doi: 10.1785/0220260124.

Supplemental Material

Introduction

Focal mechanisms (FMs) are fundamental for characterizing earthquake source processes, fault geometries, and regional stress orientations. Although moment tensor (MT) solutions provide a more complete physical description of the seismic source, their reliable estimation generally requires higher signal quality and is therefore typically limited to moderate-to-large earthquakes. As a result, first-motion polarity-based FMs remain a key tool for investigating the source properties of smaller events. However, their application to small-magnitude earthquakes is often limited by reduced waveform signal-to-noise ratios (SNRs), sparse-station coverage, and sensitivity to unmodeled structural heterogeneities (Zahradník and Sokos, 2018; Saraò *et al.*, 2021). Consequently, first-motion *P*-wave polarity-based FMs remain widely used, particularly for small earthquakes. Despite their known limitations, such as sensitivity to polarity misassignments, hypocentral uncertainties, and limited azimuthal coverage (e.g., Hardebeck and Shearer, 2002; Sabahat *et al.*, 2024), polarity-based methods provide a practical alternative when the associated uncertainties are properly quantified.

1. National Institute of Oceanography and Applied Geophysics, OGS, Trieste, Italy, https://orcid.org/0000-0002-2586-4169 (FA); https://orcid.org/0000-0001-5734-5702 (AS); https://orcid.org/0000-0002-7017-0529 (AM); https://orcid.org/0000-0002-1247-3193 (MS); https://orcid.org/0000-0002-9115-0439 (LC); https://orcid.org/0000-0002-5572-1759 (GR); https://orcid.org/0000-0001-8078-9416 (MP); 2. Department of Physics "E.R. Caianiello", University of Salerno, Fisciano, Italy, https://orcid.org/0009-0005-0480-8124 (GM); 3. Section of Naples, National Institute for Nuclear Physics (INFN), Naples, Italy

*Corresponding author: fabdi@ogs.it

Manual picking of first-motion polarities, however, is labor-intensive and subject to analyst-dependent variability, which limits its scalability for catalog enrichment and rapid-response applications. These limitations have motivated the development of automated approaches aimed at providing consistent, repeatable, and timely FM information for large volumes of seismic data.

Recent advances in automated first-motion polarity classification have substantially improved the feasibility of such workflows. Early developments, including the polarity picker introduced by Lentas (2017), enhanced the quality and completeness of first-motion data in global bulletins (Lentas and Harris, 2019; Lentas *et al.*, 2019). Since then, a wide range of automated polarity classifiers has been developed, including autoregressive approaches (Dai and MacBeth, 1995) and, more recently, deep learning-based methods. Convolutional neural networks have demonstrated strong performance in noisy conditions and across diverse tectonic settings (Ross *et al.*, 2018; Hara *et al.*, 2019), whereas unsupervised clustering techniques have shown potential for waveform characterization and quality control (Mousavi *et al.*, 2019). Supervised deep learning approaches have further been applied to polarity picking for small earthquakes (Uchide, 2020), and recent studies have integrated such classifiers into FM workflows, leading to increased polarity availability and improved solution stability (Ross *et al.*, 2018; Li *et al.*, 2023; Messuti *et al.*, 2023; Palo *et al.*, 2025; Zhang *et al.*, 2025).

Rather than introducing a new methodological framework, this study focuses on the quantitative assessment of the reliability, robustness, and operational scalability of an automated polarity-based FM workflow. The proposed workflow integrates the convolutional first motion (CFM) deep learning model for first-motion polarity classification, as implemented by Messuti *et al.* (2023), with the probabilistic SKHASH inversion algorithm (Skoumal *et al.*, 2024). Once event locations and *P*-wave arrivals are available, FMs are computed without manual polarity picking, and solution quality is evaluated through objective misfit and uncertainty metrics. The workflow is designed to ensure scalability within regional seismic networks, enabling systematic application to dense, low-magnitude seismic datasets.

We validate the workflow using an earthquake dataset with manually reviewed polarities and reference FMs (Magrin *et al.*, 2024), allowing a direct quantitative comparison between automated and analyst-derived solutions. We then apply the workflow to a dataset of approximately 1500 earthquakes ($1.0 \le M_d \le 4.6$) recorded between January 2024 and October 2025 in the southeastern Alps area of northeastern Italy, a densely populated region dominated by low-magnitude seismicity (Rebez *et al.*, 2024). Recent advances in machine learning-based detection and phase picking have enabled the systematic identification of small earthquakes in this area (Sugan *et al.*, 2023), providing a suitable basis for extending FM determination to magnitudes below the range of routine MT analysis. The resulting catalog, consisting of 122 events (Abdi *et al.*, 2026), represents the first automated FM dataset for this area and significantly densifies the available source mechanism information at magnitudes typically below the threshold of traditional analyses.

By demonstrating reliable performance on both validation and operational datasets, this study shows that automated polarity-based FM workflows can provide a practical and scalable tool for routine seismic monitoring and regional seismotectonic analysis, particularly in settings dominated by small earthquakes.

Study Area

The southeastern Alps of northeastern Italy are placed at the boundary zone between the Adriatic microplate and the Eurasian plate and represent one of the most tectonically complex and seismically active regions in Europe. This region lies near the transition between the eastern southern Alps and the northwestern Dinaric fold-and-thrust belt, where the main tectonic structures rotate from predominantly east–west (E–W) Alpine trends to northwest–southeast (NW–SE) Dinaric orientations. Deformation in this area is primarily accommodated along the southeastern Alpine thrust system, where regional shortening is absorbed at rates on the order of 1–2 mm/yr (Cheloni *et al.*, 2014; Moulin and Benedetti, 2018; Tunini *et al.*, 2024).

The interaction between Alpine compression and Dinaric structural inheritance results in a segmented and mechanically heterogeneous crust, favoring the coexistence of compressional, strike-slip, and localized extensional faulting styles. The area is characterized by a predominantly compressional to transpressional stress regime and has experienced several damaging earthquakes, including the 1976 M_w 6.4 Friuli sequence and the 1936 M_w 6.1 Bosco del Cansiglio earthquake, the latter associated with a causative fault whose geometry and segmentation remain debated (Aoudia *et al.*, 2000; Galadini *et al.*, 2005; Sugan and Peruzza, 2011). These events are associated with major thrust systems along the Alpine foothills, for which geological and geodetic studies suggest a maximum credible earthquake magnitude of up to $M_w \sim 7.5$ (Cheloni *et al.*, 2014). Seismicity in the region is predominantly concentrated at depths of approximately 5–15 km, commonly interpreted as corresponding to the deeper portion of the active thrust system near the transition between locked and creeping behavior, where interseismic strain accumulation is inferred to occur (Bressan *et al.*, 2016; Rebez *et al.*, 2024; Villani *et al.*, 2024).

Seismological monitoring in northeastern Italy is carried out through the "Sistema di Monitoraggio terrestre dell'Italia Nord Orientale (SMINO)" (see Data and Resources), operated by the Center for Seismological Research (CRS) of the National Institute of Oceanography and Applied Geophysics (OGS). The SMINO system integrates the seismic and geodetic monitoring system of northeast Italy to provide dense monitoring of the southeastern Alps and surrounding regions (Bragato *et al.*, 2021). In this study, analyses are based on waveforms from the seismic network OX complemented by data from additional Italian and international seismic networks contributing to regional monitoring (see detailed list in Data and Resources).

Earthquake locations and magnitudes are routinely reported in the bulletins of the seismometric network of northeastern Italy published online (Bulletin of the Seismometric Network of Northeastern Italy, 2025). The duration magnitude (M_d) is systematically computed for all events since 1977, whereas local (M_L) and moment magnitudes (Moratto *et al.*, 2017; Lanzoni *et al.*, 2020; Tarchini *et al.*, 2025) are reported in more recent years. For pre-2015 events, M_d is often the only available magnitude. Procedures are currently being implemented to extend magnitude information to additional source parameters (Cataldi *et al.*, 2025; Moratto *et al.*, 2026; Picozzi *et al.*, 2026). Since 2009, MT solutions have been routinely computed in near-real time for earthquakes with $M_L \geq 3.6$ (Saraò *et al.*, 2021; Sugan *et al.*, 2024). In contrast, FM information for minor events has remained sparse and largely dependent on manual first-motion analyses. Given that the seismicity in the southeastern Alps is dominated by small-magnitude earthquakes ($M_L \leq 3.5$), this limitation significantly restricts the availability of source mechanism information for the majority of recorded events.

Data

To validate the performance of the automated workflow, we analyzed a dataset spanning the period 2014–2023, with magnitudes $2.8 \leq M_d \leq 3.6$ derived from the FM catalog of Magrin *et al.* (2024), hereafter referred to as the validation dataset. In that catalog, first-motion polarity solutions were computed only for events $M_d \leq 3.6$ for which no MT solution was available. The lower boundary (M_d 2.8) reflects the availability of high-quality reference solutions from manual polarity analysis, controlled by the number of readable polarities and focal-sphere coverage (Table S1, available in the supplemental material to this article). Figure 1a shows the spatial distribution of the validation earthquakes, together with the seismic stations contributing to the analysis, highlighting the dense regional network geometry. Figure 1b,c illustrates the source-to-station distance distribution and the magnitude distribution of the validation dataset, respectively, which define the parameter space used for quantitative benchmarking of the automated workflow. This dataset is composed of approximately 6000 waveforms recorded at epicentral distances up to 200 km and corresponds to earthquakes for which high-quality focal-mechanism solutions are available. All reference FMs were computed using the FPFIT algorithm (Reasenberg and Oppenheimer, 1985) and subsequently reviewed for quality (Magrin *et al.*, 2024). First-motion polarities were obtained from manual picks and network bulletins, providing a consistent and reliable benchmark for evaluating the automated polarity classification and FM inversion workflow. The 1D velocity model of Bressan *et al.* (2003) was used for all the FM computations in both the validation and operational datasets to ensure methodological consistency.

Following this validation phase, the workflow was applied to a dataset of approximately 1500 earthquakes recorded between 1 January 2024 and 31 October 2025, with $1.0 \leq M_d \leq 4.6$. For both datasets, we analyzed vertical-component (Z) waveforms sampled or resampled at 100 Hz. When multiple vertical channels were available, the channel selection followed a fixed priority order, retaining HHZ first, then EHZ, BHZ/SHZ, and finally HNZ only when no preferred vertical channel was available. *P*-wave arrival times and hypocentral parameters were obtained from the manually revised earthquake catalog produced by the Center for Seismological Research (CRS) of OGS. In routine operations, phase picking, event detection, location, and magnitude estimation are first performed automatically using the BRTT Antelope software system and are subsequently reviewed by analysts. In this study, we directly used the final, manually revised arrival times and locations, ensuring high accuracy for polarity classification and FM inversion.

No manual modification of polarity assignments was performed for the automated dataset analyzed here. Although this work relies on revised phase information, the proposed workflow can be directly coupled with automatic phase-picking procedures, enabling operational or near-real-time FM determination without manual intervention. Station metadata, including sensor locations and instrument responses, were obtained from XML files provided by the contributing networks (see Data and Resources).

Methodology

The automated workflow implemented in this study consists of sequential steps, including waveform extraction, first-motion polarity classification, FM inversion, and quality control. The workflow (Fig. 2) integrates the CFM deep learning model for polarity classification (Messuti *et al.*, 2023) with the probabilistic SKHASH inversion algorithm (Skoumal *et al.*, 2024), using custom scripts to automate data handling and parameter exchange between the two components.

CFM is a convolutional neural network designed to classify first-motion polarities from vertical-component seismograms sampled at 100 Hz. The pretrained CFM model used in this study was originally trained on the INSTANCE dataset (Michelini *et al.*, 2021; Messuti *et al.*, 2023), which includes more than 54,000 earthquakes recorded by multiple Italian seismic networks between 2005 and 2020, spanning magnitudes from 0 to 6.5 and covering both tectonic and volcanic environments. The training dataset consists primarily of vertical-component waveforms sampled at 100 Hz from broadband and accelerometric sensors. The model operates directly on raw waveforms and outputs polarity estimates as continuous probabilities $p \in [0,1]$ representing the likelihood of upward first-motion polarity. Values close to 1 or 0 indicate high-confidence upward or downward motion, respectively,

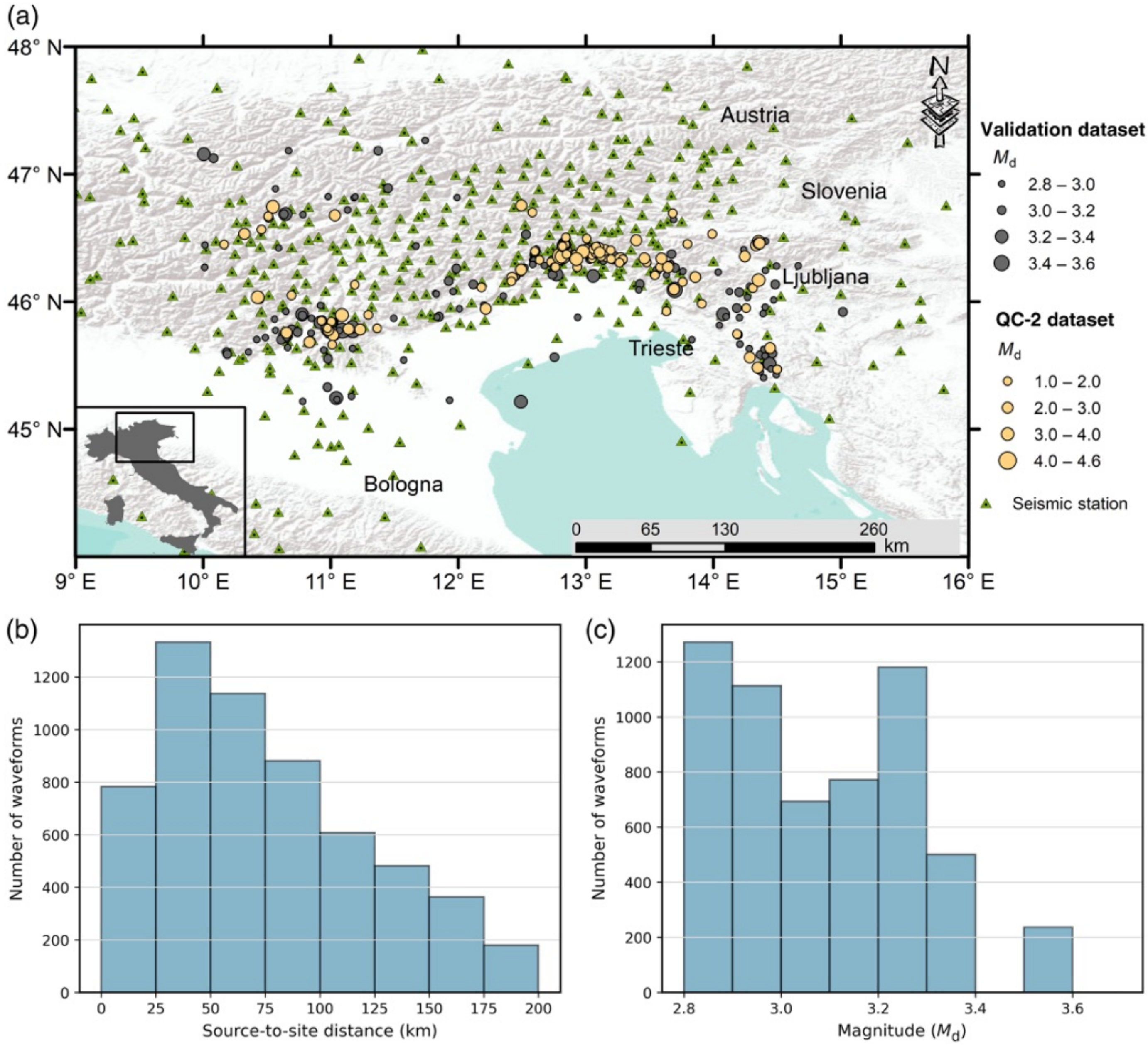

Figure 1. (a) Map of the study region, spatial distribution of earthquakes (circles) and seismic stations (green triangles). The gray circles represent the validation dataset, and yellow circles represent the location of the 2024–2025 selected data after applying the second quality control (QC-2). The inset map shows the location of the study area within Italy. Histograms show the distribution of epicentral distances between (b) events and stations and (c) earthquake magnitudes of the validation dataset. The color version of this figure is available only in the electronic edition.

whereas probabilities near 0.5 reflect low-confidence classifications typically associated with noisy signals or uncertain P-wave onsets.

For FM inversion, polarity probabilities were transformed into signed weights compatible with SKHASH using $w = 2p - 1$, mapping probabilities to the range $[-1, 1]$, where the sign indicates polarity and the magnitude reflects confidence. These weights were provided directly to SKHASH. The standard CFM implementation uses a fixed 1.6 s time window centered on a picked P-wave arrival and performs optimally when arrival times are accurate. To improve the performance under realistic operational conditions, where automatic or revised picks may include small timing uncertainties, we adopted the time-shifted version of CFM trained on windows shifted by up to ±0.1 s relative to the true onset (Messuti *et al.*, 2023). This modification increases robustness to pick time errors and distinguishes the present workflow from earlier automated polarity-based approaches that rely on fixed-window classifiers (e.g., Ross *et al.*, 2018). Before analysis, waveforms were corrected for mean and linear-trend removal, without band-pass filtering, following previous studies showing that convolutional neural networks can extract relevant multiscale features

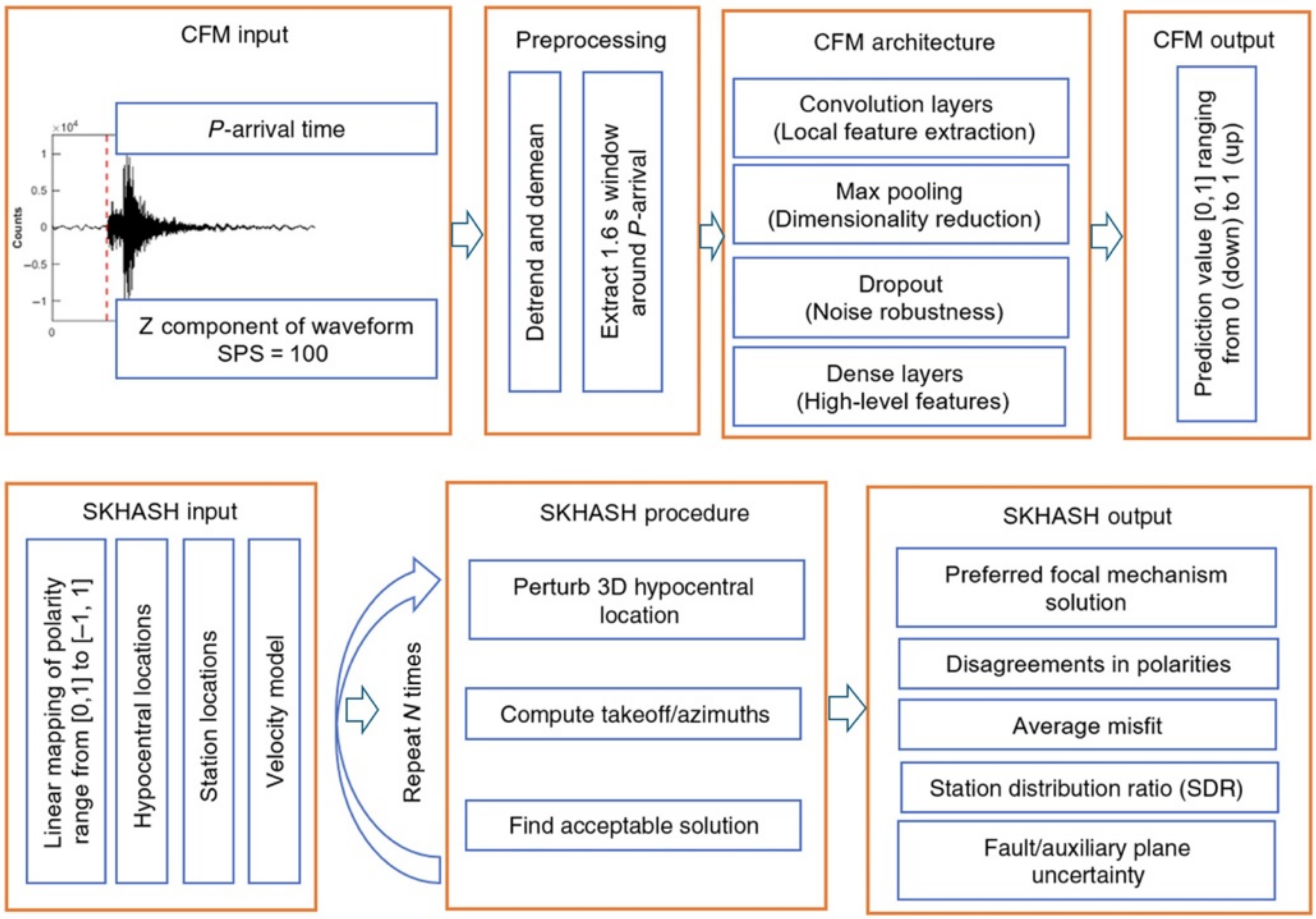

Figure 2. Flowchart diagram illustrating the automatic workflow for focal mechanism (FM) computation. It shows the sequential steps, starting with waveform and event data as input, followed by polarity classification with the convolutional first motion (CFM) neural network, and ending with FM determination using the SKHASH method. SPS, samples per second. The color version of this figure is available only in the electronic edition.

directly from broadband data and that filtering may alter first-motion polarity information (Messuti *et al.*, 2023; Yao and Zheng, 2023). The pretrained CFM model was applied without retraining or fine-tuning.

FMs were computed using SKHASH, a probabilistic extension of the HASH algorithm (Hardebeck and Shearer, 2002, 2003; Williams, 2014) that is particularly well suited for small-magnitude earthquakes. SKHASH performs a stochastic grid search over strike, dip, and rake and explicitly accounts for hypocentral uncertainty by perturbing event locations within their reported uncertainty bounds. For each perturbed realization, take-off angles are recomputed using a 1D velocity model, allowing location uncertainty to be propagated into the solution. The inversion requires first-motion polarity observations, hypocentral parameters, station coordinates, and a velocity model, and allows polarity observations to be weighted. In this study, only first-motion polarity observations were used; no amplitude-ratio constraints were included.

Solution quality was evaluated using the SKHASH quality grades (A–D), which are defined based on three diagnostic metrics: (1) average polarity misfit, (2) root mean square (RMS) nodal-plane uncertainty, and (3) station distribution ratio (SDR). The average polarity misfit represents the fraction of weighted first-motion polarities inconsistent with the preferred FM solution. RMS nodal-plane uncertainty quantifies the dispersion of acceptable strike–dip–rake solutions and reflects the stability of the inversion. The SDR measures the geometric distribution of stations in takeoff-angle space, with higher values indicating more uniform coverage and better constraint.

The threshold values adopted in this study are summarized in Table 1. For a solution to be assigned to a given quality class, all threshold criteria listed in Table 1 must be simultaneously satisfied. If one or more conditions are not met, the solution is downgraded to the next lower quality category following a hierarchical scheme. Quality control was applied at both the polarity and FM levels, and only solutions meeting the specified requirements on polarity count, azimuthal coverage, misfit, uncertainty, and station geometry were retained for the final catalog.

TABLE 1
Quality Classification Criteria Used by SKHASH for Focal Mechanism Solutions

Quality Grade	Average Misfit	RMS Plane Uncertainty	Station Distribution Ratio	Percentage of Events
A	≤0.15	≤25°	≥0.5	38.4%
B	≤0.20	≤35°	≥0.4	34.0%
C	≤0.30	≤45°	≥0.3	21.3%
D	>0.30	>45°	<0.3	6.3%

Four quality grades (A–D) are defined based on thresholds for average polarity misfit, root mean square (RMS) nodal plane uncertainty, and station distribution ratio (SDR). The table also reports the percentage of events falling into each quality grade based on the analyzed dataset.

To evaluate the operational scalability of the proposed workflow, we assessed its computational performance under typical regional-network conditions. The workflow was executed on a standard workstation equipped with an Intel Core i7-7500U central processing unit. For a typical local earthquake recorded by 20–40 stations, the total end-to-end processing time per event was on the order of 5 s, including waveform extraction and quality-control steps.

These processing times are compatible with routine operational applications within regional seismic monitoring frameworks. Once event detection, phase picking, and location are available, FM solutions can be obtained shortly thereafter without manual intervention, enabling systematic near-real-time catalog enrichment.

Validation of the Automated Workflow

To quantitatively assess the performance of the automated workflow, we applied it to the reference dataset described in the Data section, consisting of earthquakes with manually reviewed first-motion polarities and independently derived FMs.

Automated polarity classifications show strong agreement with manually reviewed picks. Overall, 92% of predicted polarities match the corresponding manual determinations. Agreement was evaluated by assigning upward polarity for $p > 0.6$ and downward polarity for $p < 0.4$, whereas intermediate probabilities ($0.4 \le p \le 0.6$) were excluded from the comparison and SKHASH inversion. The distribution of polarity probabilities is strongly bimodal, with most values clustering near 0 and 1, indicating high classification confidence (Fig. 3). Low-confidence classifications, characterized by probabilities close to 0.5, are predominantly associated with low SNRs or emergent *P*-wave onsets and are excluded from subsequent FM inversion.

To investigate the influence of seismic noise on polarity confidence, we examined the relationship between predicted polarity probability and the SNR. The SNR was computed using a 0.5 s noise window preceding the *P*-wave arrival and a 0.5 s signal window following the arrival (50 samples each at the 100 Hz sampling rate) and defined as the ratio between the mean squared amplitudes of the signal and noise windows. Figure 3 shows the average $\log_{10}$ (SNR) as a function of polarity probability, together with the number of waveforms in each probability bin. The resulting binned sequence was smoothed using a moving-average filter to emphasize the overall trend. High-confidence polarity predictions, with probabilities close to 0 or 1, are generally associated with higher average SNR values, whereas predictions in the intermediate range (0.4–0.6) correspond to significantly lower SNRs.

As an additional qualitative assessment, we visually inspected approximately 1500 waveforms spanning a wide range of noise conditions and compared polarity predictions from the time-shifted CFM variant with manual picks from Magrin *et al.* (2024). Three representative examples are shown in Figure 4, illustrating the relationship between signal quality, polarity confidence, and agreement with manual picks.

Figure 4a,b shows high-quality waveforms characterized by clear *P*-wave onsets and high SNRs. In these cases, the CFM model yields polarity probabilities close to 1, in agreement with manual polarity determinations. Figure 4c presents a lower-quality example with a more emergent onset and reduced SNR (≈ 1.5), for which the predicted polarity probability is closer to 0.5. In this case, the lower confidence reflects increased uncertainty in the first-motion polarity, despite consistency with the manual classification.

Building on the automated polarity classifications, we computed FMs for the 159 validation earthquakes (Fig. 5). All solutions are listed in Table S1. More than 72% of the solutions are classified as A or B quality (Table 1), indicating a high level of solution stability across a range of station geometries and signal conditions. As shown in Figure 5, high-quality solutions are well distributed across the study region, with no evident spatial clustering of lower-quality mechanisms, suggesting that the performance of the automated workflow is robust with respect to variations in station coverage and event location.

To quantify the agreement between the new computed FMs and the benchmark ones, we computed the Kagan angle (Kagan, 1991) for each event, which measures the 3D rotation required to align two mechanisms. Values below ∼30° are commonly interpreted as nearly identical mechanisms (e.g., Lentas and Harris, 2019). For each event, the Kagan angle was calculated between our FM solution and both nodal planes

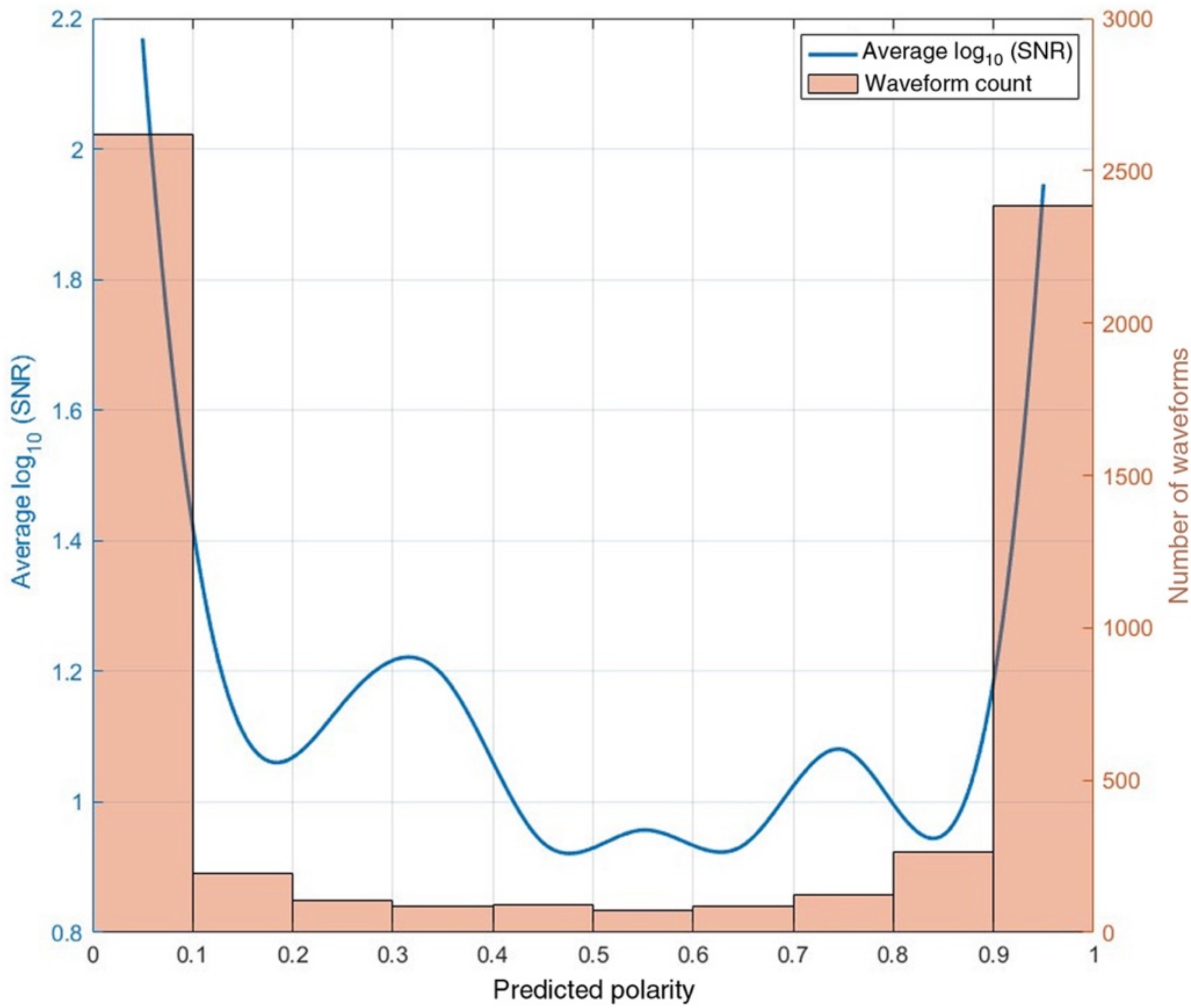

Figure 3. Dual-axis plot showing CFM prediction probabilities and associated signal-to-noise ratios (SNRs). The histogram illustrates that most predictions fall near 0 and 1, reflecting confident polarity classifications. The overlaid line graph indicates that the average $\log_{10}$ (SNR) is highest at extreme probability values and lowest around 0.5, confirming reduced model confidence under noisy conditions. The color version of this figure is available only in the electronic edition.

of the corresponding validation mechanism, retaining the smaller value as the representative misorientation (Fig. 6).

The results show that 73% of the events exhibit Kagan angles below 30°, indicating strong overall agreement between the automated and manually derived solutions. The median Kagan angle is 17.5°, with a mean of 25.3° (± 21.5°), indicating that most solutions require only modest rotations for alignment. A limited number of events display larger misorientations, in some cases approaching or exceeding 90°. Such discrepancies likely reflect a combination of factors, including differences in take-off angle estimation associated with alternative ray-tracing implementations, sensitivity to hypocentral uncertainties, and reduced polarity coverage for individual events.

To further evaluate agreement at the faulting-style level, we constructed a row-normalized confusion matrix comparing the seven Álvarez-Gómez (2019) categories derived from the automated CFM–SKHASH workflow with those of the reference catalog (Magrin *et al.*, 2024) (Fig. 6b). The matrix shows clear diagonal dominance, indicating that most events are assigned to the same faulting-style class by both approaches. Pure mechanisms, particularly reverse and normal faulting, exhibit high retention within their respective categories. Discrepancies are primarily confined to neighboring transitional classes (e.g., R versus R–SS or SS versus SS–N/SS–R), reflecting modest variations in rake partitioning rather than fundamental changes in kinematic regime. Importantly, no systematic confusion is

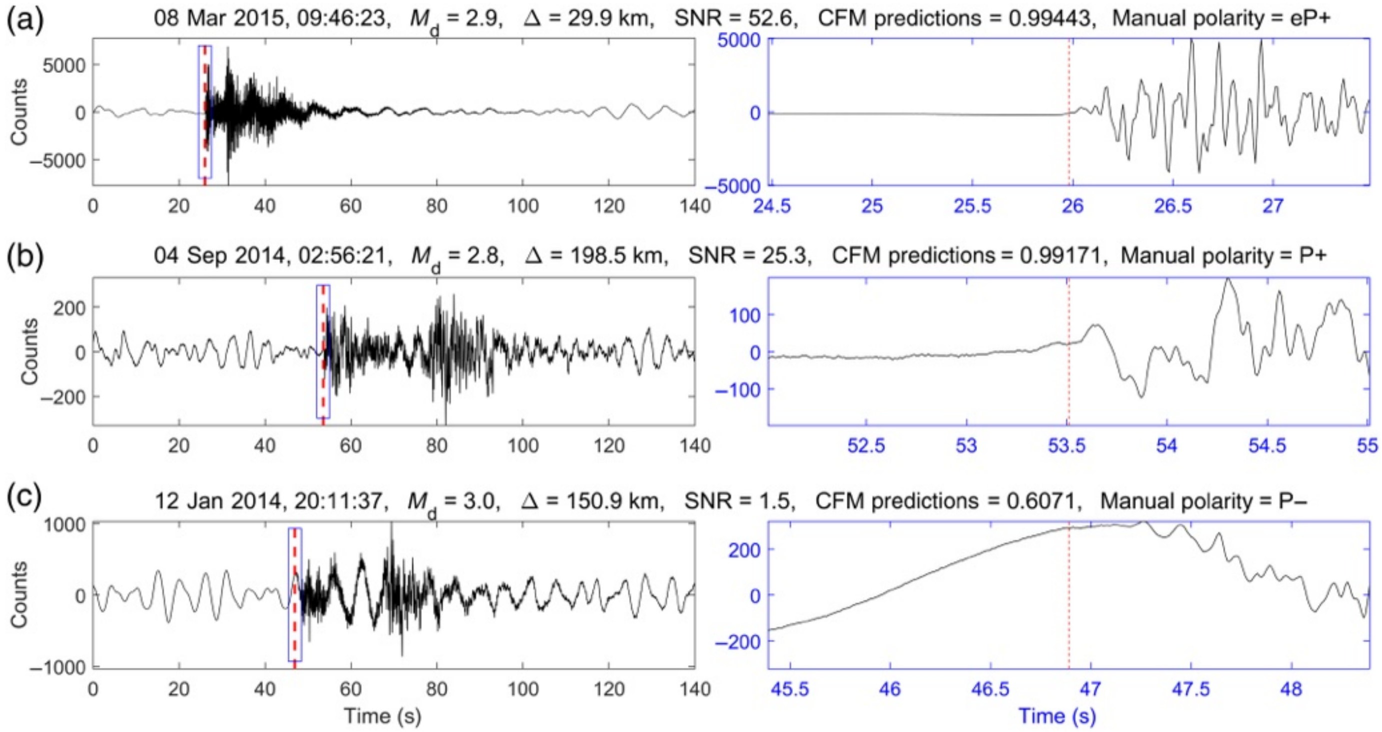

Figure 4. Example results from the CFM with time-shift model for three seismic records with varying noise levels. Each row (a–c) shows a full waveform, and in blue boxes the zoomed-in window around the *P*-wave arrival (red dashed line). Epicentral distance (Δ), magnitude (M_d), SNR, and predicted polarity are represented for each waveform. Manual polarities are labeled as *P*+ (upward) or *P*– (downward), whereas the CFM model outputs a prediction score between 0 and 1. High prediction values (close to 1 or 0) correspond to strong confidence in upward or downward polarities, respectively. As shown, examples (a) and (b) with high SNRs yield confident predictions (≥0.99), and (c), with a low SNR (1.5), results in a lower confidence prediction (0.60), illustrating the impact of noise on polarity classification. The color version of this figure is available only in the electronic edition.

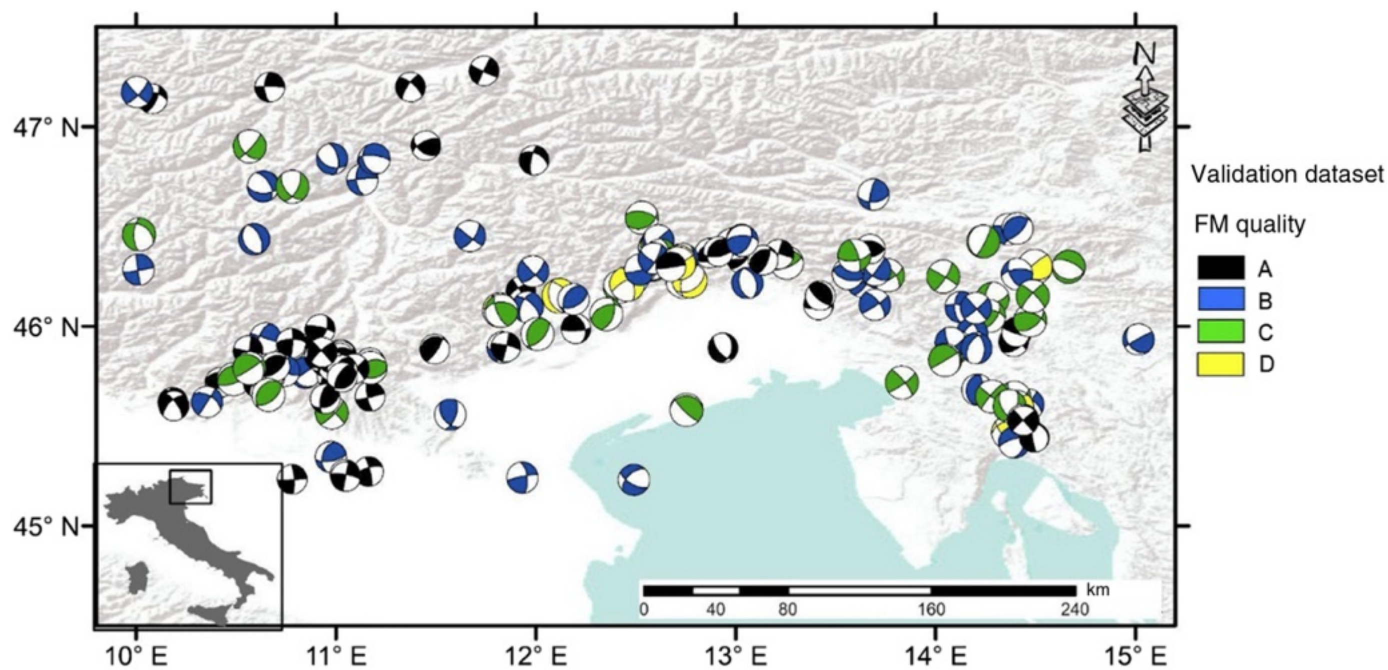

Figure 5. Automated FM solutions for 159 validation events. Mechanisms are color-coded according to SKHASH quality classes (A–D; see Table 1). The inset map shows the location of the study area within Italy. The color version of this figure is available only in the electronic edition.

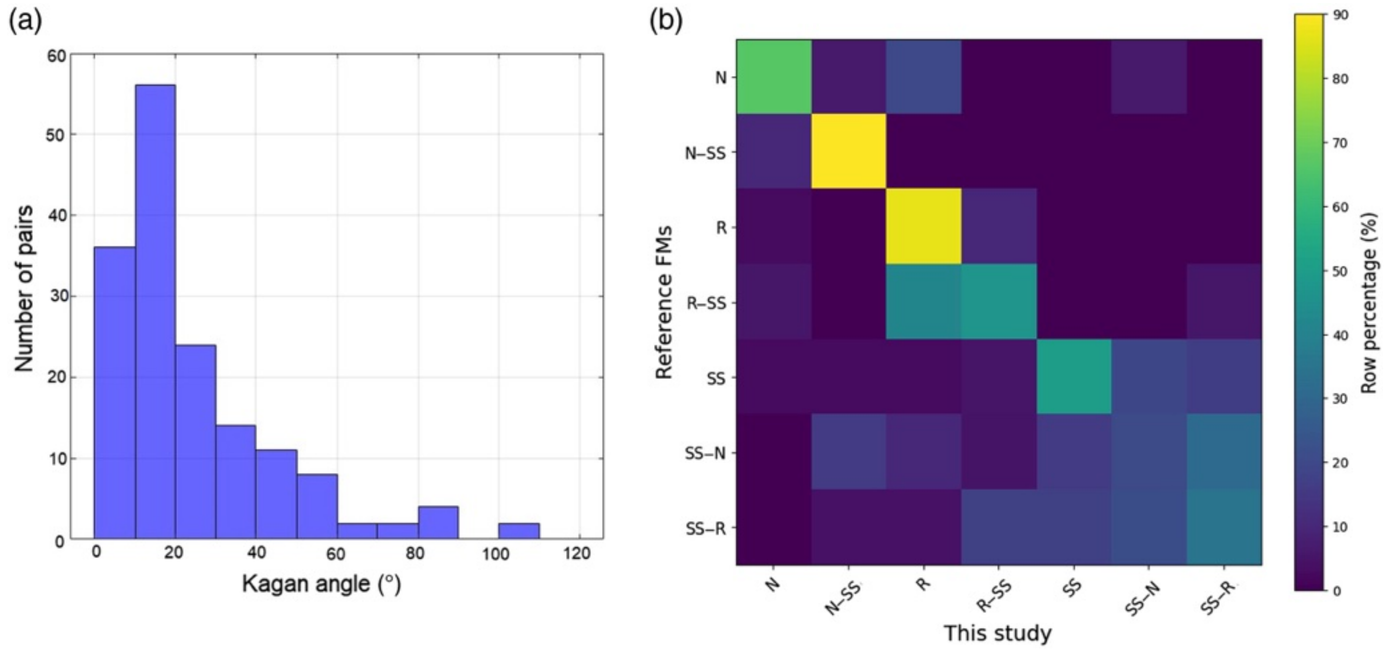

Figure 6. (a) Histogram displaying the distribution of Kagan angles for 159 earthquakes, comparing FMs derived from the automated CFM–SKHASH workflow with those obtained using FPFIT and manual polarities. (b) Row-normalized confusion matrix comparing faulting-style classifications derived in the automated CFM–SKHASH workflow with those obtained using FPFIT and manual polarities (seven classes following Álvarez-Gómez, 2019). The colors indicate the percentage of events within each reference category assigned to each class by the automated workflow. The inset map shows the location of the study area within Italy. The color version of this figure is available only in the electronic edition.

observed between pure normal and pure reverse mechanisms, confirming that the automated workflow preserves the first-order tectonic classification of the reference solutions.

Application to the 2024–2025 Seismicity: Results and Discussion

We analyzed approximately 1500 local earthquakes recorded between 1 January 2024 and 31 October 2025, with hypocentral depths ranging from 1.5 to 30 km and magnitudes M_d 1.0–4.6. All events were first subjected to waveform extraction and automated first-motion polarity classification using the CFM model. A first quality-control step was then applied to retain only events with sufficiently high-confidence polarities, adequate azimuthal coverage, and reliable hypocentral parameters. FM inversion with SKHASH was subsequently performed only for the events passing this initial screening. The resulting catalog of FMs, together with the workflow configuration parameters summarized in Table S2, is publicly available as an open dataset (Abdi *et al.*, 2026).

To define a reliable subset for FM analysis, we applied a first-stage quality control (QC-1). Events were retained only if at least twelve high-confidence *P*-wave polarities were assigned by the CFM classifier, where high confidence corresponds to polarity probabilities $p \geq 0.7$ (upward) or $p \leq 0.3$ (downward). Additional requirements included an azimuthal gap smaller than 180° and a hypocentral RMS residual below 0.5 s. After QC-1, 204 earthquakes were retained for FM inversion.

A second-stage quality control (QC-2) was adopted to obtain a conservatively selected catalog of the best-constrained FMs. Because the validation dataset covers the magnitude range $M_d \geq 2.8$, additional filtering was applied to events with M_d smaller than this value. Specifically, for the latter, only A- and B-quality solutions, as defined in Table 1, were retained, whereas all computed solutions were included for the remaining events. This additional filtering resulted in a final catalog of 122 well-constrained FMs.

We examined faulting styles, classified using the ternary P–T–B scheme of Kaverina *et al.* (1996) and the taxonomy of Álvarez-Gómez (2019). The FM distributions obtained after QC-1 and QC-2 are compared in the ternary P–T–B diagrams shown in Figure 7a,b. The QC-1 subset (Fig. 7a) exhibits a broad dispersion of solutions across the normal, strike-slip, and reverse-faulting domains, reflecting the heterogeneous nature of the initial catalog. A substantial proportion of events cluster within the normal and oblique-normal sectors, particularly at lower magnitudes, whereas strike-slip and reverse mechanisms are also represented. After applying the more stringent QC-2 selection (Fig. 7b), the overall distribution remains qualitatively similar but with reduced scatter. The removal of lower-quality solutions does not significantly alter the relative proportions of faulting styles.

The magnitude distribution of the QC-1 and of the QC-2 catalogs shows that earthquakes with $M_d \leq 2.5$ are well represented in the catalog (Fig. 7c). This significantly extends the coverage of FM data to lower magnitudes. In existing FM

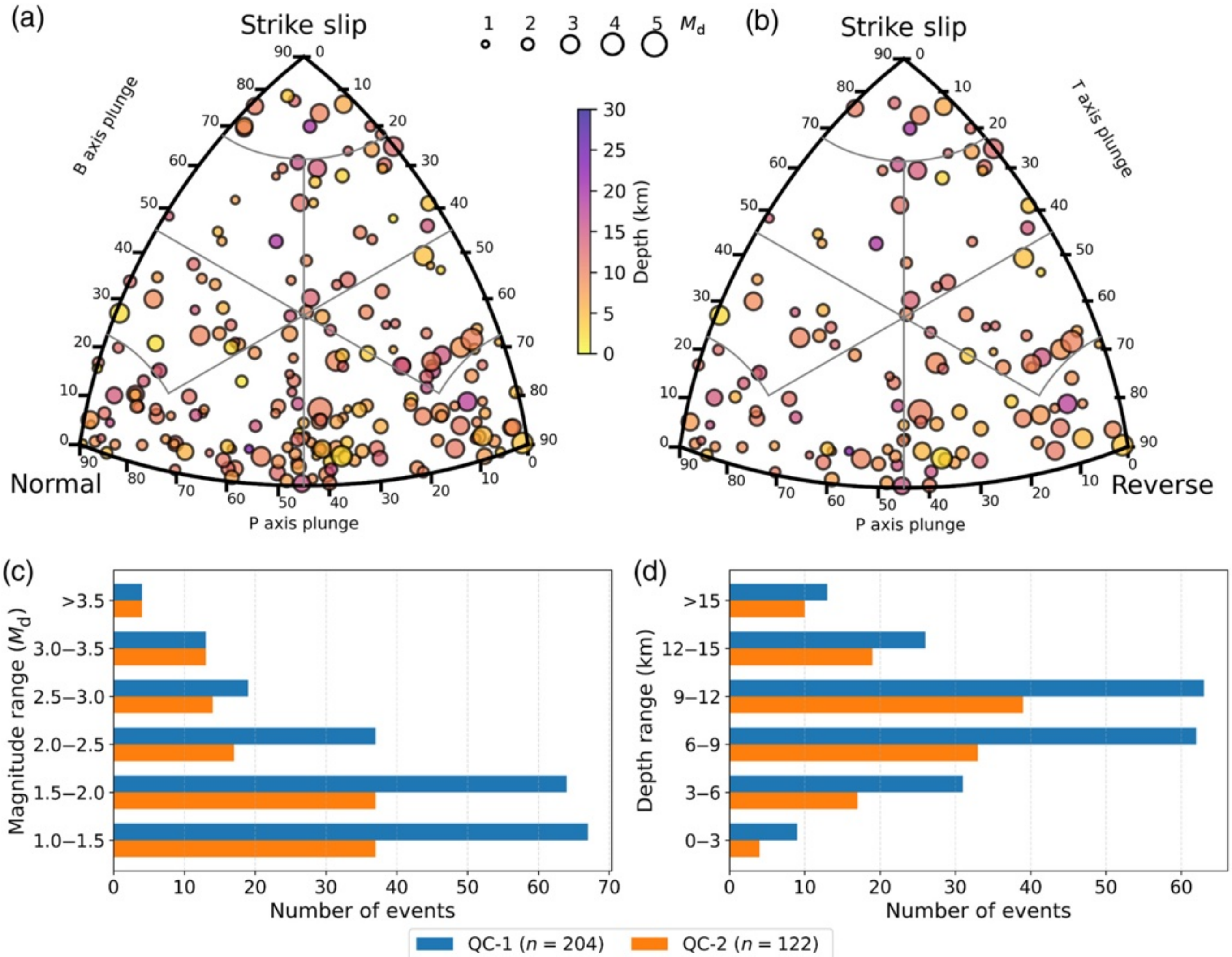

Figure 7. Distribution of FM solutions after quality control. (a,b) Ternary diagrams of focal mechanisms in P–T–B axis plunge space for the QC-1 subset (N = 204) and QC-2 subset (N = 122), respectively. Marker size scales with local magnitude (M_d), and colors represent hypocentral depth. (c,d) Magnitude and depth distributions of FM solutions for QC-1 and QC-2 subsets. QC-1 includes all events satisfying minimum requirements of polarity count, azimuthal coverage, and location quality, whereas QC-2 retains only A- and B-quality solutions according to the SKHASH classification. The diagrams illustrate the distribution of faulting styles and the effect of quality selection on the dataset. The color version of this figure is available only in the electronic edition.

catalogs for northeastern Italy (Saraò *et al.*, 2021; Sugan *et al.*, 2024), events with $M_d \leq 2.5$ account for less than 10% of the total, largely due to the limited availability of manually revised polarities for small earthquakes. In contrast, the automated workflow yields a catalog strongly dominated by small-magnitude events, with approximately 82% and 75% of the FM solutions in the QC-1 and QC-2 subsets, respectively, having $M_d < 2.5$. The automated workflow, therefore, enables a significant increase in the FM catalog at magnitudes that were previously underrepresented. Figure 7d illustrates the depth distribution of the same subsets. Seismicity is predominantly concentrated between 6 and 12 km depth, with a peak in the 9–12 km range. The depth distribution remains broadly consistent between QC-1 and QC-2, indicating that the stricter quality selection does not introduce significant depth-dependent bias. Minor reductions in the shallowest (0–3 km) and intermediate (3–6 km) bins primarily reflect the preferential removal of small, lower-quality events.

Figure 8 shows the spatial distribution of faulting styles for the QC-2 FMs. The obtained solutions reflect the structurally complex setting of northeastern Italy, located at the transition between the eastern southern Alps and the adjacent Dinaric domains.

In the eastern sector, FMs display a heterogeneous mix of normal, oblique-normal, and strike-slip solutions, consistent with previous studies documenting localized trans-tensional or extensional components superimposed on an overall compressional regime (Bressan *et al.*, 2003; Poli and Renner, 2004; Bressan and Bragato, 2009; Saraò *et al.*, 2021). This variability

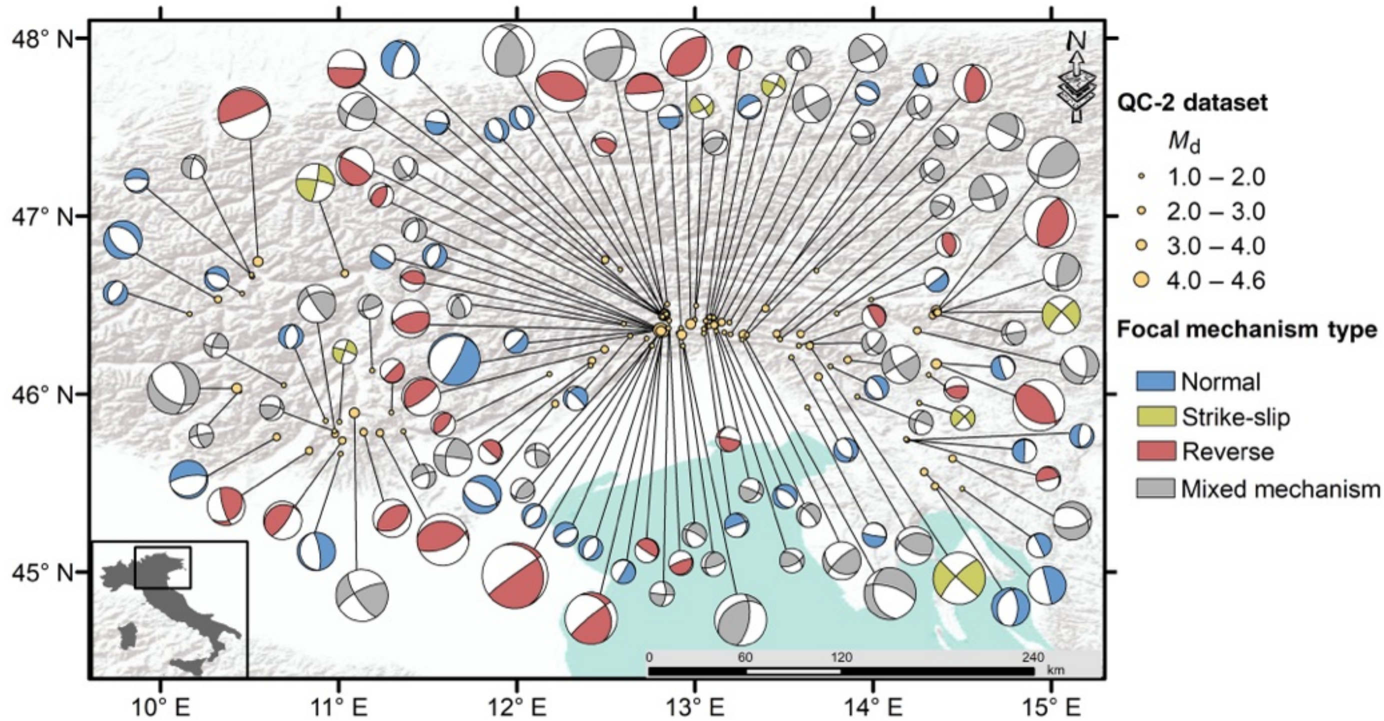

Figure 8. Spatial distribution of QC-2 FMs across the study area. Epicenters are shown by yellow filled circles, with symbol size scaled according to local magnitude (M_d). Focal mechanism plots are color-coded according to faulting style: red indicates thrust, green indicates strike-slip, blue indicates normal, and gray indicates mixed mechanisms. The inset map shows the location of the study area within Italy. The color version of this figure is available only in the electronic edition.

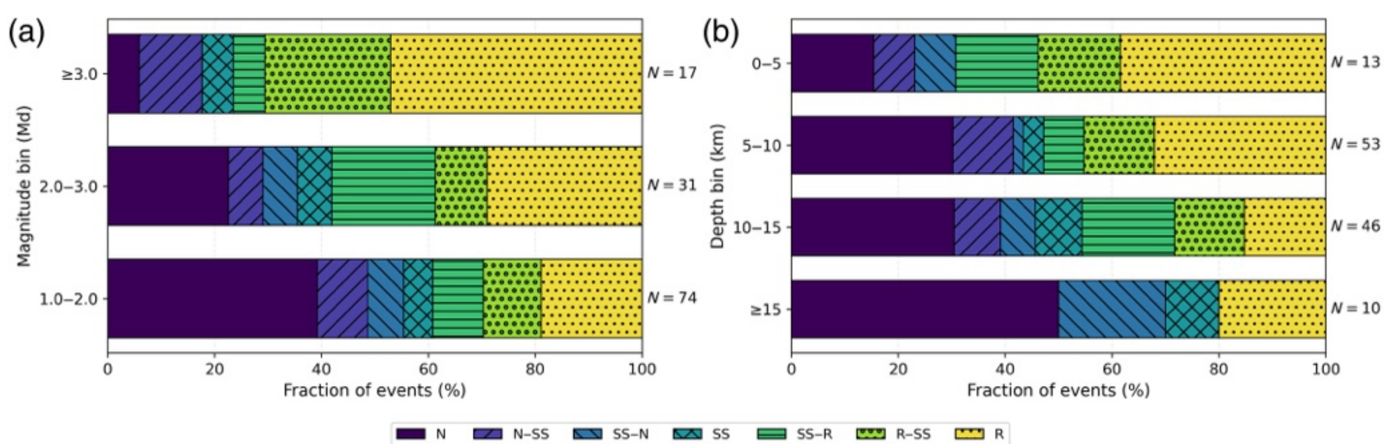

Figure 9. Faulting-style distributions for QC-2 focal mechanisms by (a) magnitude and (b) depth. The bars show the percentage of normal (N), strike-slip (SS), reverse (R), and transitional faulting-style classes within each bin; *N* indicates the number of events. The color version of this figure is available only in the electronic edition.

has been interpreted as the reactivation of inherited high-angle faults formed during earlier extensional phases, which remain mechanically viable under the present-day stress field (De Franco *et al.*, 2004; Zampieri *et al.*, 2021).

Toward the western and central sectors, closer to the Alpine thrust front, reverse and strike-slip mechanisms are more frequent, consistent with a dominantly compressional-to-transpressional regime associated with Adria–Europe convergence (Restivo *et al.*, 2016; Bressan *et al.*, 2018). Overall, the computed solutions highlight the coexistence of shortening, strike-slip deformation, and localized extensional components within a segmented orogen.

To further explore whether this spatial variability is associated with systematic differences in earthquake size or depth, the distribution of faulting styles is examined as a function of magnitude and hypocentral depth.

Figure 9 illustrates the distribution of faulting styles within the QC-2 subset as a function of magnitude (Fig. 9a) and depth (Fig. 9b). In the magnitude domain, earthquakes with M_d 1.0–2.0 (N = 74) are characterized by a comparatively higher proportion of normal and oblique-normal mechanisms, whereas strike-slip and reverse faulting become relatively more prominent at higher magnitudes. For the M_d 2.0–3.0 bin (N = 31), faulting styles are more evenly distributed, whereas reverse and oblique-reverse mechanisms represent a substantial fraction of the $M_d \geq 3.0$ bin (N = 17).

As a function of depth (Fig. 9b), FMs in the shallowest bins (0–5 km, N = 13; 5–10 km, N = 53) display mixed kinematics. In the 10–15 km interval (N = 46), compressional and strike-slip mechanisms remain well represented, whereas for the deepest bin (≥15 km, N = 10), an apparent increase in the relative contribution of normal and oblique-normal mechanisms is observed; however, any apparent increase in specific faulting styles at depth should be interpreted cautiously, given both the decreasing number of events and the larger uncertainties typically associated with hypocentral depth estimates.

Finally, it should be noted that the analyzed seismicity spans a relatively short time window (22 months), and the observed patterns reflect the deformation active during this period. Figure 9 suggests some variability in faulting style with magnitude, with M_d 1.0–2.0 events showing a relatively higher proportion of normal and oblique-normal mechanisms, whereas reverse and strike-slip components become more prominent at larger magnitudes. However, longer observation intervals and improved hypocentral locations will be required to robustly assess long-term relationships among magnitude, depth, and faulting style in this region.

2025 Raveo sequence

As an additional validation example, we analyze the 2025 Raveo earthquake sequence and compare FM solutions for six selected events with independent solutions derived from FPFIT inversion and available MT analyses.

The sequence was initiated by an M_L 3.9 event on 12 January 2025, near Udine (Fig. 10a), at a depth of about 7–10 km (Picozzi *et al.*, 2025). The mainshock was preceded by an M_L 3.7 event on 10 January and followed by an intense aftershock sequence dominated by low-magnitude earthquakes ($M_L < 2.5$), recorded by the dense SMINO monitoring network. Owing to its magnitude and societal relevance, the sequence was extensively analyzed using multiple independent methodologies, including waveform-based MT inversion for the mainshock and polarity-based FM solutions for selected larger aftershocks.

Figure 10a shows the focal mechanisms obtained using (1) FPFIT inversion with manual first-motion polarities, (2) regional MT solutions where available, and (3) the automatic CFM–SKHASH workflow. Overall, the comparison indicates consistent faulting-style classification across methods, with only minor variations in strike, dip, and rake attributable to differences in station distribution, polarity count, and inversion strategy.

In addition to computing single-event focal mechanisms, we performed a composite mechanism using the combined polarity dataset of the six events. This analysis was not intended to compensate for poorly constrained individual solutions, which are already well resolved, but rather to test the internal consistency of the polarity information within the sequence and to illustrate an additional product that the workflow can generate rapidly for clustered seismicity. The resulting composite solution (Fig. 10b) is consistent with the oblique reverse mechanism character of the sequence, while not simply reproducing the mechanism of the largest event.

Conclusions

This study provides a quantitative assessment of an automated, polarity-based FM workflow that combines deep-learning first-motion classification with probabilistic inversion to evaluate its reliability and operational applicability in a dense regional seismic monitoring context.

Benchmarking against 159 independent earthquakes with manually reviewed polarities and reference focal mechanisms demonstrates that the automated workflow reliably reproduces analyst-derived solutions. Confident polarity predictions agree with manual determinations in 92% of cases, and 73% of events exhibit Kagan angles below 30°, with a median misorientation of ∼18°. These results confirm that the automated procedure preserves the essential source characteristics of analyst-derived mechanisms.

Application of the workflow to approximately 1500 earthquakes recorded in the southeastern Alps between 2024 and 2025 yields 122 quality-controlled focal mechanisms, producing the first automated FM catalog for this region. Nearly 75% of the retained solutions correspond to earthquakes with $M_d \leq 2.5$, representing a substantial densification of the regional FM catalog at small magnitudes. Although the QC-2 subset was used here as a conservative catalog for analysis, future near-real-time releases will include the full SKHASH output and assigned quality class for all computed mechanisms, allowing users to apply their own filtering criteria for applications such as stress-tensor inversion.

The application to the 2025 Raveo earthquake sequence further confirms that the automated workflow provides FM solutions consistent with independent results derived from MT inversion and manual analyses. The close agreement across methods demonstrates that automated polarity-based approaches can reliably complement waveform-based MT solutions during active seismic sequences.

Beyond its regional implications, this study highlights the practical value of automated FM workflows for large-scale

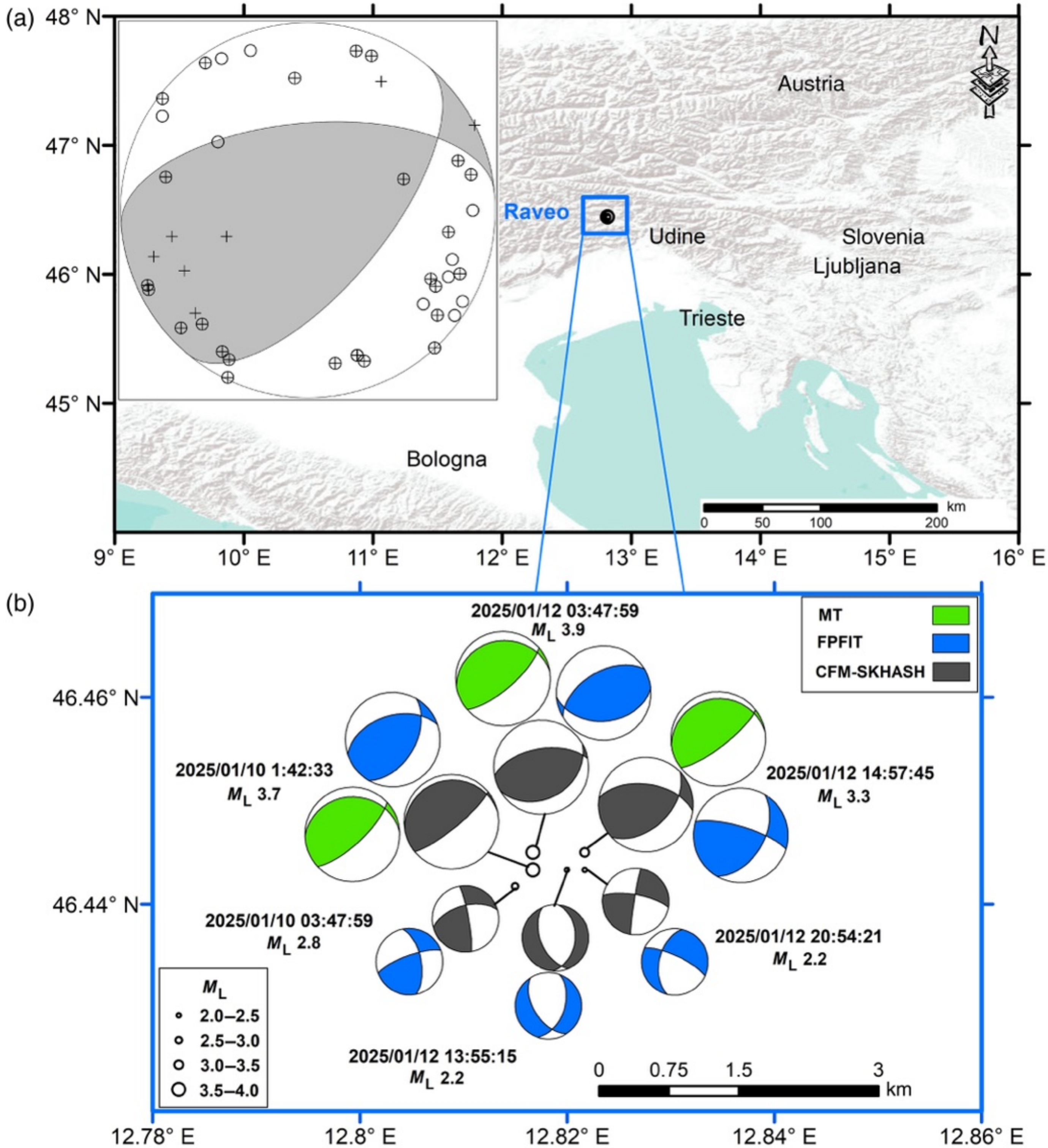

Figure 10. Methodological comparison of focal mechanism solutions for selected events within the Raveo seismic sequence. The small blue box in the regional map marks the location of the Raveo cluster in northeastern Italy. The larger blue frame outlines the zoomed area shown in panel (b), which is a map view of six events (M_L 2.2–3.9) used for cross-method comparison. FMs are color coded by inversion approach: green indicates regional moment tensor (MT) solutions, blue indicates manual polarity solutions obtained with FPFIT, and black indicates automatic solutions derived from the CFM–SKHASH workflow. (a) Composite FM computed with CFM–SKHASH using the combined polarity dataset of the six events. Polarity observations are projected onto the focal sphere according to station azimuth and takeoff angle. Plus symbols (+) denote upward first-motion polarities, whereas open circles (○) denote downward first-motion polarities. Some symbols overlap because a single station may contribute to polarity observations from more than one event included in the composite dataset. The color version of this figure is available only in the electronic edition.

and near-real-time seismic monitoring. By relying on openly available tools and clearly defined processing steps, the proposed approach is readily transferable to other regions, although some region-specific tuning may be required, and offers a scalable means of extending FM catalogs to small earthquakes. As regional catalogs continue to grow, such automated workflows provide a robust foundation for future stress-field inversions and seismotectonic investigations. Future improvements in hypocentral locations and velocity models are expected to further enhance the interpretability of automated FM catalogs and enable refined analyses of magnitude-, depth-, and faulting-style relationships.

Data Resources

The waveforms utilized in this study are recorded by the following seismic networks: 2Y (doi: 10.7914/1p36-6t87), BW (doi: 10.7914/SN/BW), CH (doi: 10.12686/sed/networks/ch), CR (doi: 10.7914/SN/CR), EV (doi: 10.7914/SN/EV), FV (doi: 10.7914/SN/FV), GR (doi: 10.25928/mbx6-hr74), GU (doi: 10.7914/SN/GU), IT (doi: 10.7914/SN/IT), IV (doi: 10.13127/SD/X0FXnH7QfY), MN (doi: 10.13127/SD/fBBBtDtd6q), NI (doi: 10.7914/SN/NI), OE (doi: 10.7914/SN/OE), OX (doi: 10.7914/SN/OX), RF (doi: 10.7914/SN/RF), SI (https://www.fdsn.org/networks/detail/SI), SL (doi: 10.7914/SN/SL), ST (doi: 10.7914/SN/ST), XT (doi: 10.15778/RESIF.XT2018), Y5 (doi: 10.12686/SED/NETWORKS/Y5), Z3 (doi:10.12686/alparray/z3_2015), Z6 (doi: 10.7914/2cat-tq59), ZO (doi: 10.13127/SD/YHCFOMCBO), and ZS (doi: 10.14470/MF7562601148). Reference focal mechanisms (FMs) used for validation are taken from the catalog of Magrin *et al.* (2024). The catalog of FMs derived in this study is publicly available through Zenodo (Abdi *et al.*, 2026). The convolutional first motion (CFM) polarity classifier (Messuti *et al.*, 2023) and the SKHASH FM inversion code (Skoumal *et al.*, 2024) are open-source software and are available from their respective repositories. The custom scripts developed in this study are used solely to automate the execution of these existing tools and to manage data input/output and are publicly available at doi: 10.5281/zenodo.18863517. All methodological choices, parameters, and quality-control criteria required to reproduce the results are fully described in the article and supplemental material. The supplemental material for this article includes two tables. Table S1 provides the validation dataset used for benchmarking the automated workflow, listing earthquake locations, magnitudes, depths, and FM parameters derived from both the CFM–SKHASH workflow and the reference catalog based on manually reviewed polarity picks and the FPFIT algorithm. A machine-readable CSV version of Table S1 is available at doi: 10.5281/zenodo.20178125. Table S2 summarizes the parameter settings adopted in the workflow, including the configuration of the CFM polarity classifier, preprocessing steps, probability thresholds, and the SKHASH inversion and quality-control parameters used in this study. Seismological monitoring in northeastern Italy is carried out through the Sistema di Monitoraggio terrestre dell'Italia Nord Orientale available at https://smino.ogs.it. All websites were last accessed in August 2026.

Declaration of Competing Interests

The authors acknowledge that there are no conflicts of interest recorded.

Acknowledgments

This research was carried out in the frame of the PRIN 2022 project "2022ZHXWC9"—Intercepting the preparatory phase of large earthquakes from seismic information and geodetic displacement and partly within the Project Monitoring Earth's Evolution and Tectonic, National Recovery and Resilience Plan (NRRP) Project Code IR0000025 under the NRRP of the Italian Ministry of University and Research funded by the European Union—NextGenerationEU. This publication has been financially supported by the European plate observing system (EPOS) Research Infrastructure through the contribution of the Italian Ministry of University and Research–EPOS ITALIA Joint Research Unit. Fatemeh Abdi supported methodology, software, data curation, formal analysis, validation, visualization, writing of the original draft, and writing of the review and editing. Angela Saraò supported conceptualization, methodology, supervision, writing of the original draft, and writing of the review and editing. Monica Sugan supported data curation, validation, and resources. Andrea Magrin supported data curation, validation, and resources. Laura Cataldi supported data curation. Giuliana Rossi supported project administration and funding acquisition. Matteo Picozzi supported project administration, funding acquisition, and supervision. All authors contributed to the evaluation, interpretation, and discussion of the results, as well as to the revision of the final article.

References

Abdi, F., A. Saraò, A. Magrin, M. Sugan, L. Cataldi, G. Messuti, G. Rossi, and M. Picozzi (2026). Focal mechanism solutions of 122 earthquakes occurred between 2024 and 2025 in the Southeastern Alps, *Zenodo*, doi: 10.5281/zenodo.20178125.

Álvarez-Gómez, J. A. (2019). FMC – Earthquake focal mechanisms data management, cluster and classification, *SoftwareX* **9,** 299–307, doi: 10.1016/j.softx.2019.03.008.

Aoudia, A., A. Saraó, B. Bukchin, and P. Suhadolc (2000). The 1976 Friuli (NE Italy) thrust faulting earthquake: A reappraisal 23 years later, *Geophys. Res. Lett.* **27,** 573–576, doi: 10.1029/1999GL011071.

Bragato, P. L., P. Comelli, A. Saraò, D. Zuliani, L. Moratto, V. Poggi, G. Rossi, C. Scaini, M. Sugan, C. Barnaba, *et al.* (2021). The OGS-north-eastern Italy seismic and deformation network: Current status and outlook, *Seismol. Res. Lett.* **92,** no. 3, 1704–1716, doi: 10.1785/0220200372.

Bressan, G., and P. L. Bragato (2009). Seismic deformation pattern in the Friuli-Venezia Giulia region (north-eastern Italy) and western Slovenia, *Boll. Geofis. Teor. Appl.* **50,**, 255–275.

Bressan, G., C. Barnaba, P. L. Bragato, M. Ponton, and A. Restivo (2018). Revised seismotectonic model of NE Italy and W Slovenia based on focal mechanism inversion, *J. Seismol.* **22,** no. 6, 1563–1578, doi: 10.1007/s10950-018-9785-2.

Bressan, G., P. L. Bragato, and C. Venturini (2003). Stress and strain tensors based on focal mechanisms in the seismotectonic framework of the Friuli–Venezia Giulia region (north-eastern Italy), *Bull. Seismol. Soc. Am.* **93,** 1280–1297, doi: 10.1785/0120020058.

Bressan, G., M. Ponton, G. Rossi, and S. Urban (2016). Spatial organization of seismicity and fracture pattern in NE Italy and W Slovenia, *J. Seismol.* **20,** 511–534, doi: 10.1007/s10950-015-9541-9.

Bulletin of the Seismometric Network of Northeastern Italy (2025). Available at http://www.crs.ogs.it/bollettino_new/ (last accessed May 2025).

Cataldi, L., M. Picozzi, M. D'Amico, P. Morasca, D. Bindi, V. Poggi, G. Costa, A. Viganò, and D. Spallarossa (2025). Supplements to "Stress drop and seismic efficiency distributions over the Adriatic indenter (European Southeastern Alps).", *Zenodo*, doi: 10.5281/zenodo.15052353.

Cheloni, D., N. D'Agostino, and G. Selvaggi (2014). Interseismic coupling, seismic potential, and earthquake recurrence on the southern front of the Eastern Alps (NE Italy), *J. Geophys. Res. Solid Earth* **119,** no. 5, 4448–4468, doi: 10.1002/2014JB010954.

Dai, H., and C. MacBeth (1995). Automatic picking of seismic arrivals in local earthquake data using an artificial neural network, *Geophys. J. Int.* **120,** 758–774, doi: 10.1111/j.1365-246X.1995.tb01851.x.

De Franco, R., G. Bressan, and G. F. Gentile (2004). Elastic moduli and seismogenic aspects of the Friuli upper crust, *Boll. Geofis. Teor. Appl.* **45,** 145–164, doi: 10.4430/bgta0113.

Galadini, F., M. E. Poli, and A. Zanferrari (2005). Seismogenic sources potentially responsible for earthquakes with M ≥ 6 in the eastern southern Alps (Thiene-Udine sector, NE Italy), *Geophys. J. Int.* **161,** no. 3, 739–762, doi: 10.1111/j.1365-246X.2005.02571.x.

Hara, S., Y. Fukahata, and Y. Iio (2019). P-wave first-motion polarity determination of waveform data in western Japan using deep learning, *Earth Planets Space* **71,** no. 1, doi: 10.1186/s40623-019-1111-x.

Hardebeck, J. L., and P. M. Shearer (2002). A new method for determining first-motion focal mechanisms, *Bull. Seismol. Soc. Am.* **92,** no. 6, 2264–2276, doi: 10.1785/0120010200.

Hardebeck, J. L., and P. M. Shearer (2003). Using S/P amplitude ratios to constrain the focal mechanisms of small earthquakes, *Bull. Seismol. Soc. Am.* **93,** no. 6, doi: 10.1785/0120020236.

Kagan, Y. Y. (1991). 3-D rotation of double-couple earthquake sources, *Geophys. J. Int.* **106,** no. 3, doi: 10.1111/j.1365-246X.1991.tb06343.x.

Kaverina, A. N., A. V. Lander, and A. G. Prozorov (1996). Global creepex distribution and its relation to earthquake-source geometry and tectonic origin, *Geophys. J. Int.* **125,** 249–265, doi: 10.1111/j.1365-246X.1996.tb06549.x.

Lanzoni, A., L. Moratto, E. Priolo, and M. A. Romano (2020). Fast Mw estimation of microearthquakes recorded around the underground gas storage in the Montello-Collalto area (Southeastern Alps, Italy), *J. Seismol.* **24,** 1029–1043, doi: 10.1007/s10950-019-09889-0.

Lentas, K. (2017). Towards routine determination of focal mechanisms obtained from first motion P-wave arrivals, *Geophys. J. Int.* **212,** no. 3, 1665–1686, doi: 10.1093/gji/ggx503.

Lentas, K., D. Di Giacomo, J. Harris, and D. A. Storchak (2019). The ISC Bulletin as a comprehensive source of earthquake source mechanisms, *Earth Syst. Sci. Data* **11,** 565–578, doi: 10.5194/essd-11-565-2019.

Lentas, K., and J. Harris (2019). Enhanced performance of ISC focal mechanism computations as a result of automatic first-motion polarity picking optimization, *J. Seismol.* **23,** 1141–1159, doi: 10.1007/s10950-019-09862-x.

Li, S., L. Fang, Z. Xiao, Y. Zhou, S. Liao, and L. Fan (2023). FocMech-flow: Automatic determination of P-wave first-motion polarity and focal mechanism inversion and application to the 2021 Yangbi earthquake sequence, *Appl. Sci.* **13,** 2233, doi: 10.3390/app13042233.

Magrin, A., M. Sugan, A. Snidarcig, M. A. Romano, M. Guidarelli, M. Santulin, P. Di Bartolomeo, and A. Saraò (2024). Focal mechanism solutions of 162 earthquakes occurred between 2014 and 2023 in the Southeastern Alps, *Zenodo*, doi: 10.5281/zenodo.10851786.

Messuti, G., S. Scarpetta, O. Amoroso, F. Napolitano, M. Falanga, and P. Capuano (2023). CFM: A convolutional neural network for first-motion polarity classification of seismic records in volcanic and tectonic areas, *Front. Earth Sci.* **11,** doi: 10.3389/feart.2023.1223686.

Michelini, A., S. Cianetti, S. Gaviano, C. Giunchi, D. Jozinović, and V. Lauciani (2021). INSTANCE – the Italian seismic dataset for machine learning, *Earth Syst. Sci. Data* **13,** 5509–5544, doi: 10.5194/essd-13-5509-2021.

Moratto, L., F. Abdi, and A. Saraò (2026). Seismic source parameters analysis in southeastern Alps and associated tectonic implications, *Tectonophysics* doi: 10.1016/j.tecto.2026.231069.

Moratto, L., A. Saraò, and E. Priolo (2017). Moment magnitude (M_w) estimation of weak seismicity in northeastern Italy, *Seismol. Res. Lett.* **88,** 1455–1464, doi: 10.1785/0220170063.

Moulin, A., and L. Benedetti (2018). Fragmentation of the Adriatic promontory: New chronological constraints from Neogene shortening rates across the Southern Alps (NE Italy), *Tectonics* **37,** 3328–3348, doi: 10.1029/2018TC004958.

Mousavi, S. M., W. Zhu, W. Ellsworth, and G. Beroza (2019). Unsupervised clustering of seismic signals using deep convolutional autoencoders, *IEEE Geosci. Remote Sens. Lett.* **16,** no. 11, doi: 10.1109/LGRS.2019.2909218.

Palo, M., O. Amoroso, F. Napolitano, G. Messuti, and S. Scarpetta (2025). An automatic workflow to infer focal mechanisms of micro-earthquakes: Application to Southern Italy, *IEEE J. Sel. Top. Appl. Earth Observ. Remote Sens.*, doi: 10.1109/JSTARS.2025.3624231.

Picozzi, M., F. Abdi, C. Barnaba, M. Bertoni, P. L. Bragato, P. Brondi, L. Caravella, G. Capotosti, L. Cataldi, P. Comelli, *et al.* (2025). Rapporto di sintesi sul Terremoto di Raveo ML 3.9 del 12 Gennaio 2025 (Udine), doi: 10.5281/zenodo.15168324.

Picozzi, M., L. Cataldi, A. Viganò, G. Ferretti, P. Brondi, D. Bindi, A. Magrin, G. D. Chiappetta, A. G. Iaccarino, D. Scafidi, *et al.* (2026). Seismic energy from small earthquakes maps fault segmentation in the southeastern Alps, *Sci. Rep.*, doi: 10.1038/s41598-026-35618-y.

Poli, M. E., and G. Renner (2004). Normal focal mechanisms in the Julian Alps and Prealps: Seismotectonic implications for the Italian-Slovenian border region, *Boll. Geofis. Teor. Appl.* **45,** 51–69.

Reasenberg, P., and D. Oppenheimer (1985). FPFIT, FPPLOT and FPPAGE: Fortran computer programs for calculating and displaying earthquake fault-plane solutions, *U.S. Geol. Surv. Open File Rept. 85-739*, 109 pp.

Rebez, A., G. Renner, D. Sandron, and D. Slejko (2024). The eastern Alps earthquake catalogue 513 (1977–2022), *Bull. Geophys. Oceanogr.* **65,** 115–122, doi: 10.4430/bgo00453.

Restivo, A., G. Bressan, and M. Sugan (2016). Stress and strain patterns in the Venetian Prealps (north-eastern Italy) based on focal-mechanism solutions, *Boll. Geofis. Teor. Appl.* **57,** 13–30, doi: 10.4430/bgta0166.

Ross, Z. E., M. A. Meier, and E. Hauksson (2018). P wave arrival picking and first-motion polarity determination with deep learning, *J. Geophys. Res. Solid Earth* **123,** no. 6, doi: 10.1029/2017JB015251.

Sabahat, S., M. Tahir, F. Munir, B. Saif, M. T. Iqbal, J. Iqbal, and T. Iqbal (2024). Inversion techniques for focal mechanism determination of small-magnitude earthquakes: A comparative study using the Burewala earthquake (M_w ~ 4) in Pakistan, *J. Seismol.* **28,** 119–131, doi: 10.1007/s10950-023-10186-0.

Saraò, A., M. Sugan, G. Bressan, G. Renner, and A. Restivo (2021). A focal mechanism catalogue of earthquakes that occurred in the Southeastern Alps and surrounding areas from 1928–2019, *Earth Syst. Sci. Data* **13,** no. 5, doi: 10.5194/essd-13-2245-2021.

Skoumal, R. J., J. L. Hardebeck, and P. M. Shearer (2024). SKHASH: A Python package for computing earthquake focal mechanisms, *Seismol. Res. Lett.* **95,** no. 4, 2519–2526, doi: 10.1785/0220230329.

Sugan, M., and L. Peruzza (2011). Distretti sismici del Veneto, *Boll. Geofis. Teor. Appl.* **52,** 3–90, doi: 10.4430/bgta0057 (in Italian).

Sugan, M., L. Peruzza, M. A. Romano, M. Guidarelli, L. Moratto, D. Sandron, M. P. Pleasencia Linares, and M. Romanelli (2023). Machine learning versus manual earthquake location workflow: Testing LOC-FLOW on an unusually productive microseismic sequence in northeastern Italy, *Geomat. Nat. Hazard. Risk* **14,** no. 1, doi: 10.1080/19475705.2023.2284120.

Sugan, M., A. Saraò, A. Magrin, A. Snidarcig, G. Bressan, G. Renner, M. A. Romano, M. Guidarelli, M. Santulin, P. Di Bartolomeo, *et al.* (2024). Focal mechanisms of the Southeastern Alps and surroundings (2.0), *Zenodo*, doi: 10.5281/zenodo.10853582.

Tarchini, G., L. Moratto, and A. Saraò (2025). A comprehensive moment magnitude catalog for the Northeastern Italy region, *Seismol. Res. Lett.* **2025,** doi: 10.1785/0220240303.

Tunini, L., A. Magrin, G. Rossi, and D. Zuliani (2024). GNSS time series and velocities about a slow convergent margin processed on HPC clusters: Products and robustness evaluation, *ESSD*, **16,** 1083–1106, doi: 10.5194/essd-16-1083-2024.

Uchide, T. (2020). Focal mechanisms of small earthquakes beneath the Japanese islands based on first-motion polarities picked using deep learning, *Geophys. J. Int.* **223,** no. 3, doi: 10.1093/gji/ggaa401.

Villani, F., A. Antonioli, M. Pastori, P. Baccheschi, and M. G. Ciaccio (2024). Stress patterns and crustal anisotropy in the Eastern Alps: Insights from seismological and geological observations, *Tectonics* **43,** e2023TC008033, doi: 10.1029/2023TC008033.

Williams, M. C. (2014). HASHpy, *Zenodo*, doi: 10.5281/zenodo.9808.

Yao, K., and Y. Zheng (2023). Fundamentals of machine learning, in *Springer Series in Optical Sciences*, Vol. 241, doi: 10.1007/978-3-031-20473-9_3.

Zahradník, J., and E. Sokos (2018). Moment tensor resolvability: Application to the weak events of the South Aegean, *Bull. Seismol. Soc. Am.* **108,** no. 2, 816–830, doi: 10.1785/0120170246.

Zampieri, D., P. Vannoli, and P. Burrato (2021). Geodynamic and seismotectonic model of a long-lived transverse structure: The Schio-Vicenza Fault System (NE Italy), *Solid Earth* **12,** 1967–1986, doi: 10.5194/se-12-1967-2021.

Zhang, C., J. Zhang, and J. Zhang (2025). Deriving focal mechanism solutions of small to moderate earthquakes in Sichuan, China via a deep learning method, *Earthq. Res Adv.* **5,** 100371, doi: 10.1016/j.eqrea.2025.100371.

Manuscript received 9 March 2026
Published online 22 September 2026